J. Fluid Mech. (1991), *vol.* 231, *pp.* 501–528
Printed in Great Britain

Onset of three-dimensionality, equilibria, and early transition in flow over a backward-facing step

By LAMBROS KAIKTSIS†, GEORGE EM KARNIADAKIS AND STEVEN A. ORSZAG

Mechanical and Aerospace Engineering and Applied and Computational Mathematics, Princeton University, Princeton, NJ 08544, USA

(Received 30 March 1990 and in revised form 8 April 1991)

A numerical study of three-dimensional equilibria and transition to turbulence in flow over a backward-facing step is performed using direct numerical solution of the incompressible Navier–Stokes equations. The numerical method is a high-order-accurate mixed spectral/spectral-element method with efficient viscous outflow boundary conditions. The appearance of three-dimensionality in nominally two-dimensional geometries is investigated at representative Reynolds numbers ranging from the onset of three-dimensional bifurcation to later transitional stages. Strongly three-dimensional regions are identified through standard correlation coefficients and new three-dimensionality indices, as well as through instantaneous and time-average streamline patterns and vorticity contours. Our results indicate that onset of three-dimensionality occurs at the boundaries between the primary and secondary recirculating zones with the main channel flow, the latter being the most stable flow component. There is, therefore, strong secondary instability in the shear layers, mainly due to the one emanating from the step corner.

The flow further downstream is excited through the action of the upstream shear layers acquiring a wavy form closely resembling Tollmien–Schlichting waves both spatially and temporally with a characteristic frequency f_1; upstream, at the shear layer another incommensurate frequency, f_2, is present. The two-frequency flow locks-in to a single frequency if external excitations are imposed at the inflow at a frequency close to f_1 or f_2; the smaller amplitude excitations, however, may cause a strong quasi-periodic response. Such excitations may significantly increase or decrease (by more than 20%) the length of the primary separation zone X_R at lock-in or quasi-periodic states. The equilibrium states resulting from the secondary instability at supercritical Reynolds numbers produce a flow modulated in the spanwise direction, with corresponding variations in the reattachment location X_R. While three-dimensionality explains partially the discrepancy between numerical predictions and experimental results on X_R at higher Reynolds number Re, the main source of discrepancy is attributed to the inflow conditions, and in particular to external disturbances superimposed on the mean flow, the latter being the main reason also for the somewhat earlier transition found in laboratory experiments.

1. Introduction

In the past decade there have been substantial developments in our understanding of transition to turbulence with solutions given to some longstanding questions in a number of fundamental flows. Most of the work in the past few years has focused on

† Current address: Institut für Energietechnik, ETH-Zentrum, Zurich, Switzerland.

the early transition regime of simple-geometry flows, where novel stability theory in conjunction with direct numerical computations have elucidated the role of secondary instability (Orszag & Patera 1983) in the transition process. Initially, secondary instability was explored for the plane Poiseuille flow; today, however, this is a well-established transition scenario and its validity has been verified for pipe flows, boundary layers (Herbert 1988), and open shear flows (Pierrehumbert & Widnall 1982; Metcalfe *et al.* 1987). The apparently universal character of the secondary instability at subcritical Reynolds numbers, preceding an abrupt transition to turbulence, has only been realized for flows with simple (non-inflexional) mean profiles. Recent stability calculations in complex-geometry flows (Karniadakis & Amon 1987; Karniadakis, Mikic & Patera 1988) have shown that, unlike the planar shear flows, complex-geometry flows exhibit supercritical transitions, and that steady three-dimensional equilibrium states can be achieved (Karniadakis 1990). In addition, multiple physical interactions occurring among the many different flow regions (e.g. streamwise locations with inflexional and fully developed flow profiles) with variable stability properties make these flows very different from the simple parallel shear flows studied in detail so far.

Advancing our understanding of transition in complex geometry flows requires building a database of transition characteristics of prototype flows. We suggest that the flow over a backward-facing step can serve as such a prototype. It consists of three main flow components: the shear layer emanating from the step edge, the separation zone at the channel expansion, and the fully developed channel flow further downstream. This flow has received tremendous attention in the last three decades (see Denham & Patrick 1974 and Armaly *et al.* 1983, and references therein) and has served as a model of massive flow separation in internal flows as induced by sudden changes in the geometry. The emphasis has been mostly on the laminar and fully turbulent flow regime where transport measures such as shear stress and heat transfer rates were measured and correlated (Aung & Goldstein 1972; Vogel & Eaton 1984). A more systematic set of measurements in the transitional regime, which is of interest to us here, was obtained by Armaly *et al.* (1983) where mean, first-order quantities were measured for Reynolds numbers up to $Re = 8000$ (a fully turbulent regime).

The large amount of available experimental data stimulated a number of numerical studies (Osswald, Ghia & Ghia 1983; Patera 1984; Kim & Moin 1985; Sethian & Ghoniem 1988; Ku *et al.* 1989). In the low-Reynolds-number regime a unique relationship exists between the Reynolds number (Re), the expansion ratio (r), and the normalized length of the recirculation zone (X_R/S), so that new numerical methodologies can readily be tested. In the high-Reynolds-number regime the recirculation zone length is uniquely determined by the expansion ratio, so similar tests have been performed to validate turbulence models and related methodologies (see Karniadakis *et al.* 1989, and references therein).

Our interest in the present work is in studying three-dimensionality and steady equilibrium states of a wall-bounded separated flow in a nominally two-dimensional geometry; hence, the backward-facing step is a prototype. In decomposing the flow into its fundamental components we can think of the entire field as represented by a (convectively unstable) inflexional profile just downstream of the step and a fully recovered parabolic profile in the far field. The question we address therefore is how and in what parameter range this idealized model is most susceptible to two- and three-dimensional instabilities. Indeed, the bifurcation of the steady, two-dimensional laminar flow to three-dimensional flow is likely to be the primary source

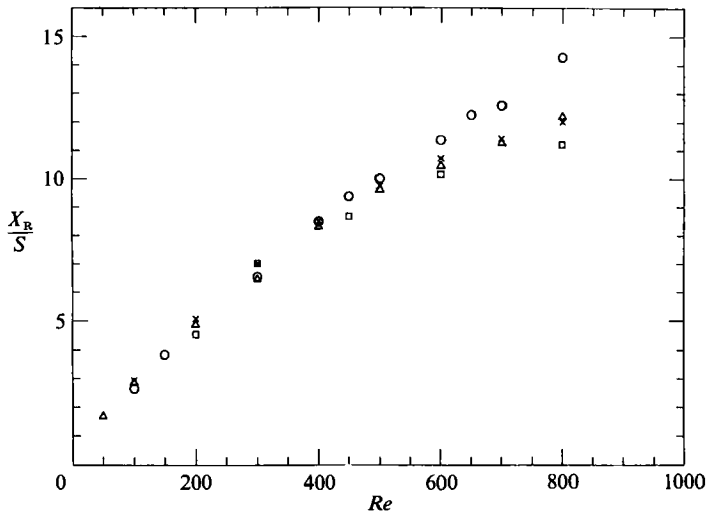

FIGURE 1. Recirculation length, X_R, normalized by step height, S, versus Reynolds number Re for experiment and two-dimensional simulations: ○, experimental data (Armaly *et al*); ×, Kim & Moin; □, Osswald *et al.*; △, present work.

of discrepancies appearing in comparisons of (two-dimensional) numerical predictions and experimental data above a characteristic Reynolds number. In figure 1, we summarize the numerical results of two-dimensional calculations done by several investigators corresponding to different methodologies; also included are the experimental data of Armaly *et al.* (1983) for the same step geometry with expansion ratio $r = 1.94$. Indeed, we observe that irrespective of the numerical approach followed, there exists a consistent underestimation of the recirculation length X_R above Reynolds number $Re \approx 600$.

Bifurcation to three-dimensionality, however, depends strongly on the location; while mean velocity profiles located upstream are inflexional and correspond to two- and three-dimensional growth rates that are almost equal in magnitude, parabolic profiles in the downstream channel section are characterized by a more hierarchical bifurcation process. In the latter case a primary instability leading to an oscillatory state is followed by the secondary instability. Therefore, in order to quantify globally the three-dimensionality of the entire field, it is appropriate to introduce pointwise indices to measure the spanwise inhomogeneity and spanwise correlations; these indices should be carefully measured and/or computed. The temporal response and structure of separated flows is also a strong function of the disturbance level. Unsteadiness can lead to completely altered flow patterns as has been demonstrated in the complex-geometry flows studied by Ghaddar *et al.* (1986) and Karniadakis *et al.* (1988). Controlled experiments, therefore, which focus on these specific issues are needed.

In this work, we use a high-order numerical method extended here to three-dimensions to address these questions and provide answers in a systematic and quantitative form through detailed numerical experimentation. A similar methodology has been used in the past to study highly unsteady, two-dimensional free-shear and wall-bounded shear flows (Karniadakis & Triantafyllou 1989; Karniadakis *et al.* 1988; Ghaddar *et al.* 1986).

The paper is organized as follows. In §2, we present the governing equations and introduce the numerical methodology employed for our investigation; a more

detailed discussion and related references are given in the Appendix. In §3, we present results of two- and three-dimensional simulations for steady and unsteady flow fields. In §4, we discuss in detail the flow structure and quantify the spanwise variation of the flow using three-dimensionality indices. In §5, the effect of external excitations, of non-parabolic inflow profiles, as well as the effect of no-slip wide walls is investigated. Finally, in §6 we summarize the results and present a possible scenario of three-dimensionality and early transition of the flow over a backward-facing step and relate it to the transition of shear layers and plane channel flows.

2. Methodology

We consider Newtonian fluids governed by the Navier–Stokes equations of motion and subjected to the incompressibility condition,

$$\frac{\mathrm{D}\boldsymbol{v}}{\mathrm{D}t} = -\frac{\nabla p}{\rho} + Re^{-1}\nabla^2 \boldsymbol{v} \quad \text{in} \quad \Omega, \tag{1a}$$

$$\nabla \cdot \boldsymbol{v} = 0 \quad \text{in} \quad \Omega, \tag{1b}$$

where $\boldsymbol{v}(\boldsymbol{x}, t)$ is the velocity field, p is the static pressure, and the Reynolds number Re is defined as $Re = \frac{2}{3}U_{\max}(2h)/\nu$; here all lengths are non-dimensionalized with h the height of the inlet channel. Also, $U_{\max}$ is the maximum velocity at the inlet, ν is the kinematic viscosity, and ρ is the density; D denotes total derivative.

The numerical solution of the above system of equations will be obtained in the domain Ω shown in figure 2. The step has a (non-dimensional) height $S = 0.94231$, while the spanwise length is $L_z = 2\pi$ corresponding to wavenumber $\beta = 1$. In most of the calculations presented here we assume periodic boundary conditions in the spanwise direction (boundary Γ_s), while a parabolic velocity is prescribed at the inflow boundary Γ_i. In §4 we examine the effect of non-parabolic inflow profiles, as well as the effect of no-slip at the sidewalls. At the downstream boundary mixed Neumann/viscous-sponge boundary conditions (Tomboulides, Israeli & Karniadakis 1991) are prescribed which eliminate spurious numerical instabilities at the outflow even for very high-Reynolds-number flow and provide better accuracy than the previously employed extrapolation outflow boundary conditions (Karniadakis & Triantafyllou 1989).

The above system of equations (1) is solved by employing three-dimensional spectral-element discretizations in the domain Ω and high-order splitting schemes for the time integration. A brief review of both discretizations as well as a detailed list of related literature can be found in the Appendix.

3. Numerical simulations

3.1. *Two-dimensional simulations*

In this Section, simulations of the two-dimensional flow are presented corresponding to a parabolic inflow profile imposed at approximately one step height upstream of the step expansion. Experimentation with the parabolic profile imposed at different upstream locations results in negligible differences in the flow field, unless the Reynolds number is very low ($Re \leqslant 200$); for $Re \leqslant 200$, the value of X_R is overpredicted by almost 10% if the inflow boundary is taken exactly at the step expansion. To investigate the effect of the outflow, here we consider two different domains corresponding to outflow length $X_O = 34$ and $X_O = 60$) (see figure 2*a*).

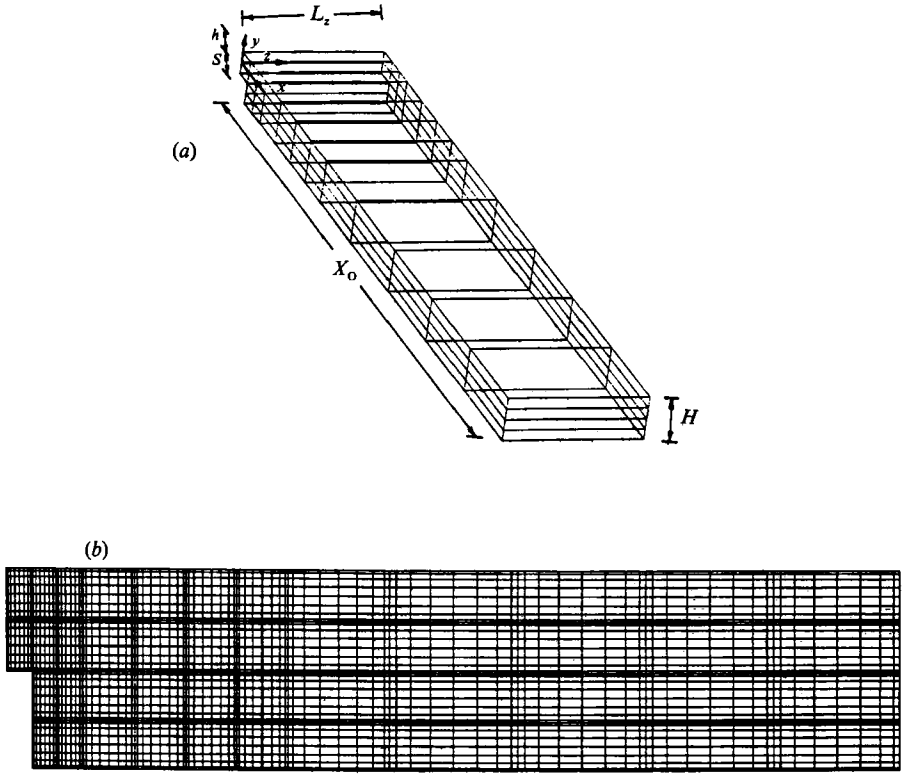

FIGURE 2. (*a*) Sketch of the step geometry defining various geometrical parameters. A skeleton of the three-dimensional spectral element decomposition of the domain is indicated. (*b*) Spectral-element discretization of an (x, y)-plane. The same discretization applies on all planes $z = \text{const.}$ (The x and y scales are not the same; here $S = 0.94$, and typically $X_0 = 34$.)

Again, the flow is affected very little in the lower-Reynolds-number regime, while for $Re \geqslant 700$ differences in the value of X_R of approximately 2% were observed. Finally, experimentation with higher resolution per spectral element (using eleventh-order polynomial expansions instead of eighth) produced identical results for all simulations, indicating that the spatial resolution employed is sufficient for the range of Reynolds number considered here ($Re \leqslant 1300$). Regarding time accuracy, tests with schemes of order $J = 2$ and $J = 3$ (see Appendix) as well as time step $\Delta t = 10^{-2}$ and 10^{-3} resulted in differences of approximately 1%. Typical two-dimensional runs required 10000 time steps (30 min on a Cray-Y/MP1); three-dimensional cases (§3.2) were typically run in increments of 3000 time steps (1 h on a Cray-Y/MP1). A more detailed discussion of validation tests can be found in Kaiktsis (1990).

The flow over the backward-facing step considered here is two-dimensional and non-oscillatory at $Re \leqslant 500$. This was verified in our three-dimensional simulations, where initial spanwise disturbances introduced into the flow decayed exponentially to zero; the experimental findings by Armaly *et al.* also support our conclusion. In figure 3 we plot the steady-state streamline pattern, where we see that in addition to the primary recirculation zone there exists a secondary separation zone near the upper wall due to the adverse pressure gradient caused by the sudden expansion at the step edge. The flow recovers rapidly downstream to a parabolic profile. In the laminar regime the recirculation length X_R scales with the Reynolds number, i.e.

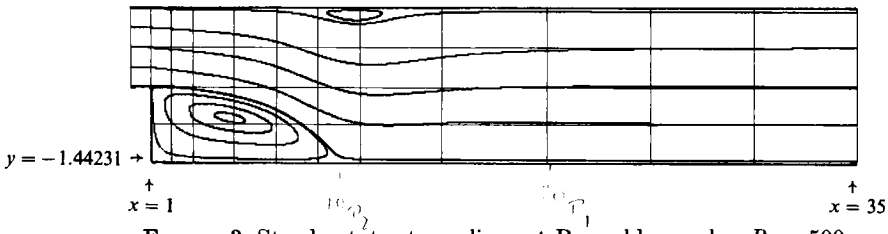

FIGURE 3. Steady-state streamlines at Reynolds number $Re = 500$.

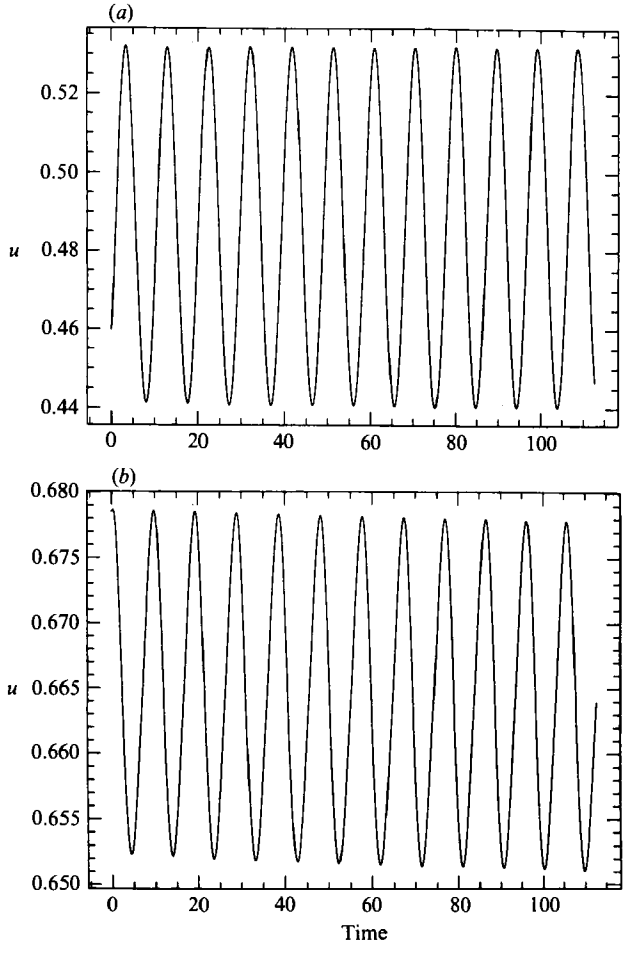

FIGURE 4. Time history of streamwise velocity component at $Re = 700$. (*a*) Downstream point P_1 ($x = 20.3$; $y - 0.821$); (*b*) upstream point P_2 ($x = 10.4$; $y = -0.650$).

$X_R/S \propto Re^m$. The exponent m decreases with the expansion ratio $r = H/h$; for $r = 1.94$, $m(r = 1.94) \approx 0.75$. For other values of r the values of m obtained with our simulations coincide with the results of Thangam & Knight (1989).

At Reynolds number $Re = 700$ the flow has already undergone its first bifurcation. In figures 4(*a*) and 4(*b*) we plot the time history of the streamwise velocity at the point P_1 located at ($x = 20.3$; $y = -0.821$) downstream in the channel section, and at

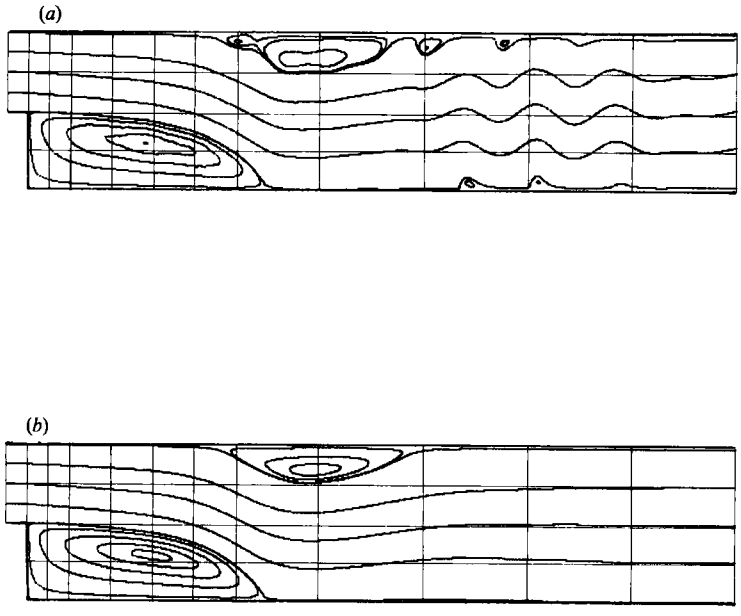

FIGURE 5. Streamlines at $Re = 800$: (*a*) instantaneous flow, (*b*) time-average flow.

the upstream point P_2 located at $(x = 10.4; y = -0.650)$, respectively. The frequency of the oscillation is the same at these points (as well as at various other points we traced between locations) with value $f_2 = 0.104$.

The flow remains oscillatory as we increase the Reynolds number. In figure 5 (*a*) we plot the instantaneous streamline pattern after a steady oscillatory state has been reached. The size of both the lower and upper wall bubbles are significantly increased, while smaller size vortices are detached, shed from the walls, and convected by the main flow. However, the time-average flow (see figure 5*b*) corresponds to a fully developed channel flow downstream, while the secondary bubble near the upper wall slightly shrinks in size. The fact that the size of the time-average primary separation zone remains essentially unchanged from its instantaneous size indicates that the velocity–pressure fluctuations are significantly smaller in this region – the leeward face of the step. At this Reynolds number and at the point P_1 in the channel section, the power spectrum exhibits a single peak corresponding to a new lower frequency $f_1 = 0.054$ (figure 6*a*), while at the upstream point P_2 the power spectrum reveals the existence of a second frequency $f_2 = 0.104$ (figure 6*b*), apparently associated with the shear layer emanating from the step edge. This frequency has exactly the same value as the one identified at the lower Reynolds number $Re = 700$. The third peak shown in figure 6 (*b*) is identified as a linear combination of f_1, f_2, i.e. $\frac{1}{2}(f_1 - f_2)$. Careful examination of power spectra corresponding to various other locations upstream as well as downstream reveals no other fundamental frequencies of the system distinct from linear combinations of f_1, f_2. Comparison of the temporal response at the two Reynolds numbers therefore suggests that the flow has undergone a second bifurcation at $Re = 800$.

The coexistence of two incommensurate frequencies at the relatively low Reynolds number $Re = 800$ is of course consistent with the fact that this is a spatially developing flow exhibiting a very different spatial structure downstream. Indeed, the perturbation field in the wavy part of the flow (figure 7) shown here in the form of

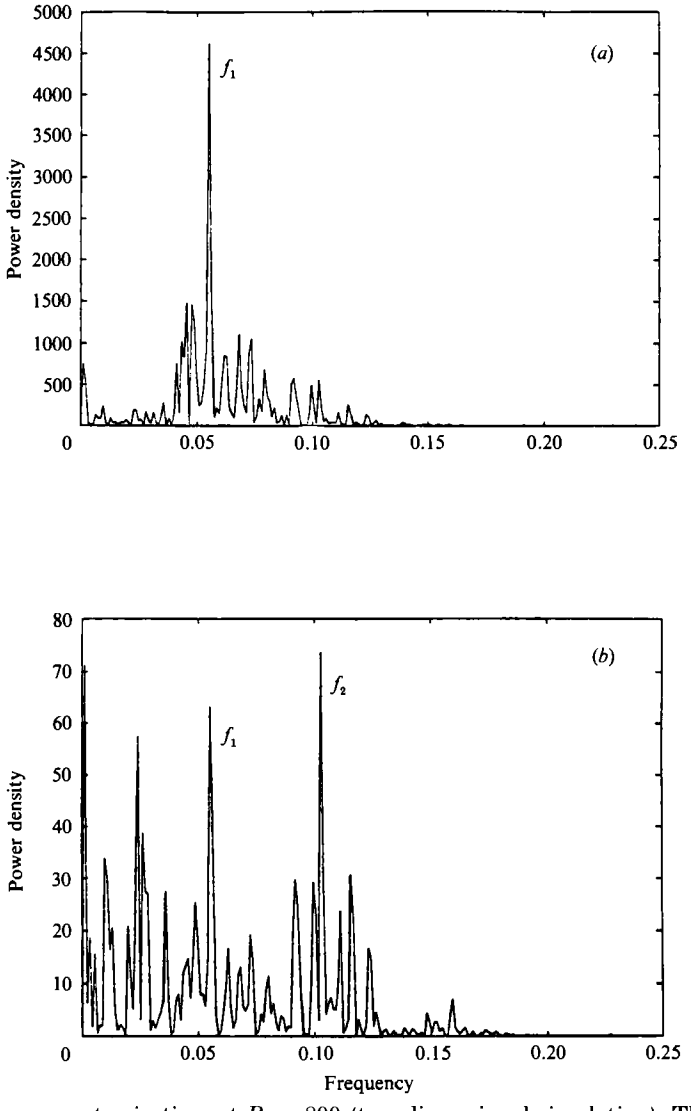

FIGURE 6. Power spectra in time at $Re = 800$ (two-dimensional simulation). The units are the natural units based on the computation. (*a*) Downstream point P_1, (*b*) upstream point P_2.

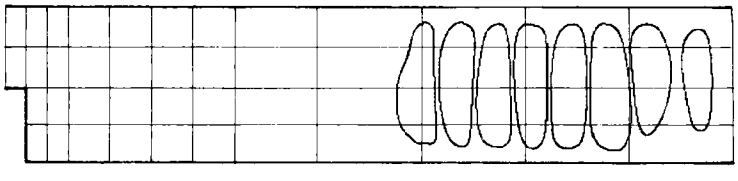

FIGURE 7. Streamlines of the time-fluctuating velocity field $\boldsymbol{v}'$ in the downstream region ($x > 20$; $Re = 800$; two-dimensional simulation). Here $\boldsymbol{v}' = \boldsymbol{v} - \bar{\boldsymbol{v}}$, where $\bar{\boldsymbol{v}}$ is the time-average velocity. These streamline patterns resemble those of channel Tollmien–Schlichting waves.

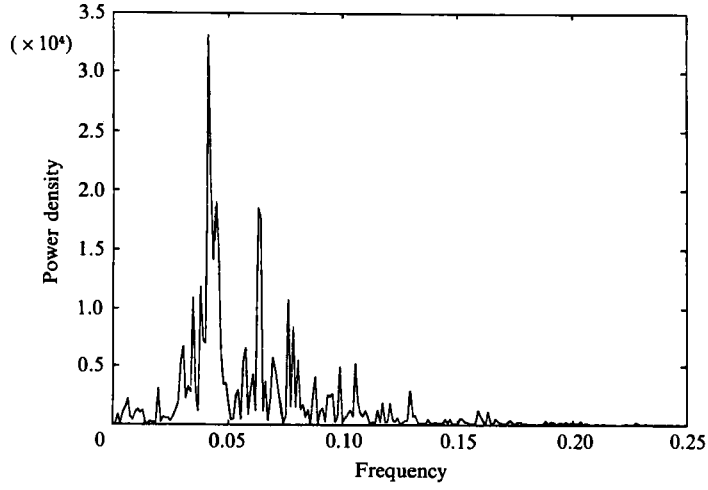

FIGURE 8. Power spectrum in time at $Re = 1095$ at the downstream point P_1 (two-dimensional simulation).

instantaneous streamlines for $x \geqslant 20$ exhibits close resemblance with channel Tollmien–Schlichting (T–S) waves corresponding to a streamwise wavenumber $\alpha = 1.605$. An eigenvalue temporal analysis employing the Orr–Sommerfeld equation (Orszag 1971) gives an eigenfrequency for the least-stable eigenmode to within 10% from $f_1 = 0.054$ computed through direct simulation of the entire flow field. The corresponding growth rate of T–S waves at this Reynolds number predicted by the Orr–Sommerfeld equation is $\sigma = -0.1045$, indicating stable subcritical behaviour. In a plane channel therefore under identical conditions these T–S waves are not present; however, in the step geometry these 'native', subcritical T–S waves are triggered by the unstable shear layer emanating upstream. This instability of the shear layer, which occurs at low Reynolds number can drastically change the growth rate of the subcritical T–S waves downstream (making σ positive), while only slightly modifying their eigenfrequency (by approximately 10%). This seems to be a universal behaviour in complex-geometry wall-bounded flows as first suggested by Karniadakis & Amon (1987) for streamwise periodic flows; here we verify that such behaviour is also valid for wall-bounded spatially developing flows.

At higher Reynolds number the power spectra are more wideband and it is therefore difficult to identify dominant frequencies in as clear a way as for $Re = 800$. At Reynolds number $Re = 1095$ (figure 8), for example, the power spectrum of the streamwise velocity at the point P_1 downstream still exhibits a maximum at the corresponding T–S eigenfrequency shifted to a lower value in accordance with the prediction of the Orr–Sommerfeld equation. However, the presence of other frequencies of smaller amplitude is also seen with the most pronounced one identified as $\frac{1}{2}f_2$, the latter being shifted somewhat. Perhaps the most important difference in the flow field at this Reynolds number is that the dominant frequency everywhere in the field (upstream locations included) is the channel frequency f_1; for example at point P_2 the power density at f_2 is only $\frac{1}{4}$ of the power density peak at f_1.

Our results suggest that the transition process starts at approximately $Re \approx 700$ with fluctuations becoming increasingly larger as Re approaches 1000. This effect is illustrated in figures 9(*a*) and 9(*b*), where we plot the histogram of the vertical

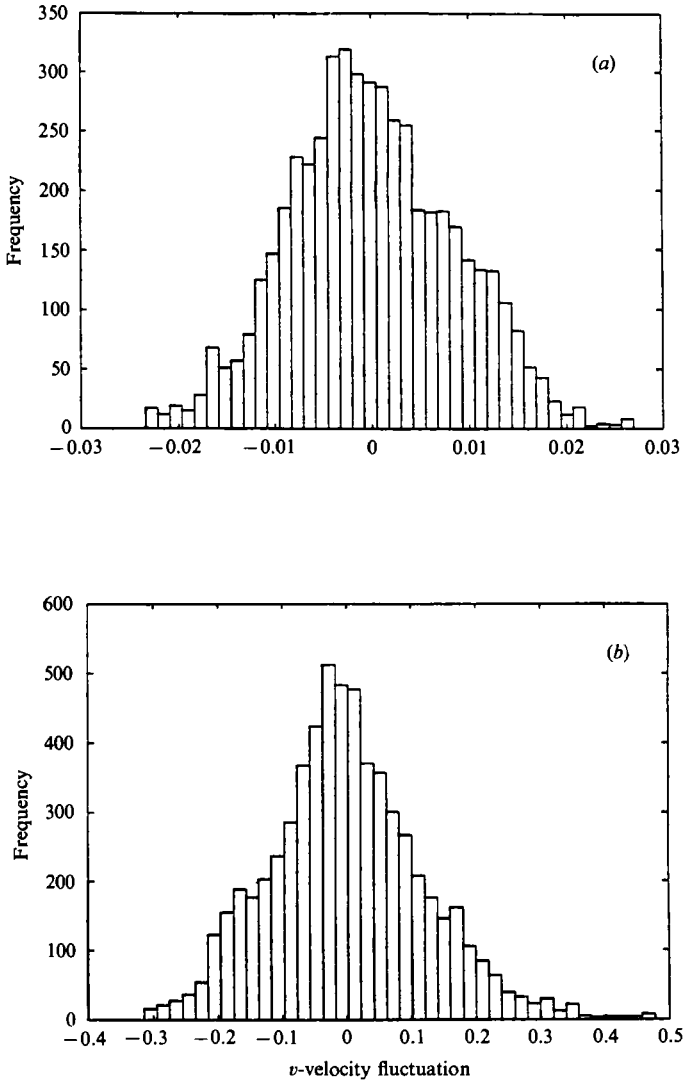

FIGURE 9. Histogram of v-velocity fluctuations (y-direction) in the shear-layer region at P_2 (two-dimensional simulation): (*a*) $Re = 800$, (*b*) $Re = 1095$.

component of velocity fluctuations (y-component) of point P_2 in the shear-layer region at $Re = 800$ and 1095, respectively. In the latter case, the width of the distribution is larger by an order of magnitude.

3.2. *Three-dimensional simulations*

Systematic experimentation employing both two- and three-dimensional simulations suggests that the flow first becomes oscillatory at $Re_c \approx 700$. This Reynolds number is higher than the one found in the experiment of Armaly *et al.* (1983). However, this is justifiable since the exact critical Reynolds number Re_c is strongly influenced by the existence of external, uncontrollable disturbances in the physical experiment (see §5). In order to approximately determine Re_c, a number of simulations were run with an initial perturbation imposed as an external forcing for some initial period and removed thereafter, following the time trace of all velocity components at later

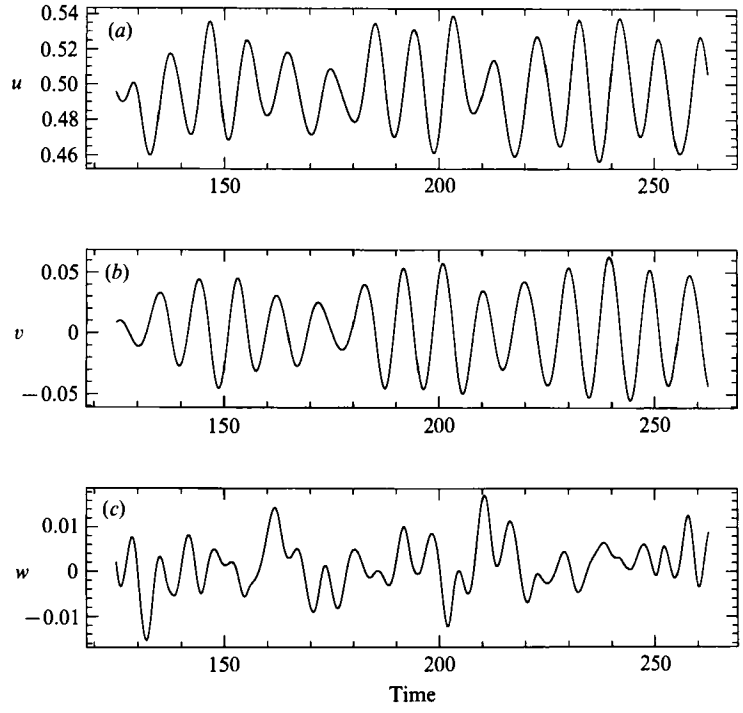

FIGURE 10. Time trace of velocity components at downstream point P_1 at $Re = 700$: (*a*) streamwise component, (*b*) vertical component, (*c*) spanwise component.

times. Similarly, for the three-dimensional simulations an initial perturbation is imposed in the third direction and subsequently the response of the flow is followed in time.

At subcritical Reynolds numbers all initial perturbations in the velocity field decay to zero. Time traces at $Re = 620$ of the spanwise component reveal a rapid decay to zero suggesting that the flow returns to two-dimensionality (Kaiktsis 1990). Cross-examination of the other two velocity components suggests in addition that the flow reaches a time-independent state. At higher Reynolds numbers, all velocity components vary in time as seen in figure 10(*a–c*), where the three velocity components at P_1 are plotted at $Re = 700$. These oscillations have a bounded amplitude suggestive of the existence of stable three-dimensional states. The frequency of these oscillations is $f_2 = 0.104$, exactly the same as that predicted in two-dimensional simulations at the same Reynolds number. It is, therefore, shown here that the primary bifurcation practically coincides with the secondary one, at which the flow becomes three-dimensional. This transition process of the flow from steady two-dimensional laminar states to unsteady three-dimensional ones should be attributed to the upstream inflexional part of the flow which, according to linear stability results, corresponds to two- and three-dimensional growth rates of almost equal magnitude (Metcalfe *et al.* 1987). This process is very different from the transition in wakes (Karniadakis & Triantafyllou 1991) where the critical Reynolds number for the secondary bifurcation is four to five times the critical Reynolds number of the primary bifurcation, suggesting a hierarchy of transition stages.

Next we simulate the flow at $Re = 800$. A qualitative description of the flow field is given in figure 11(*a–d*) (plate 1) in terms of instantaneous streamlines. In figure

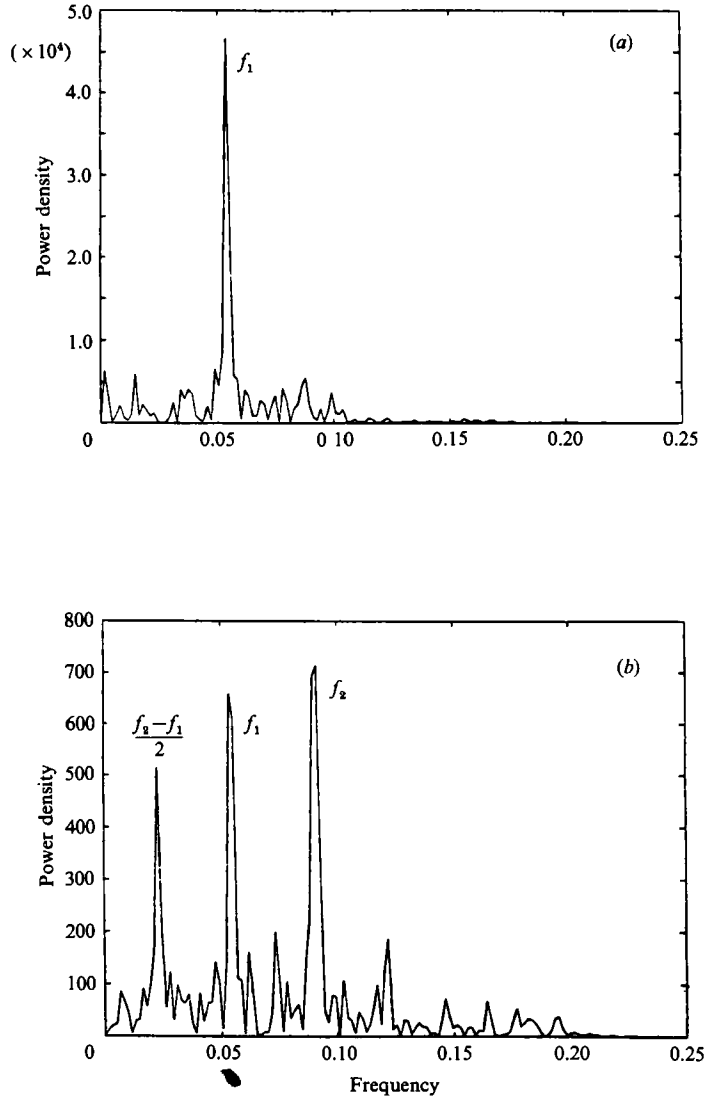

FIGURE 12. Power spectra in time at $Re = 800$ (three-dimensional simulation). (*a*) Downstream point P_1, (*b*) upstream point P_2.

11(*a*), a three-dimensional view of the streamlines emanating from the same vertical position ($y = 0$) is shown. This plane is essentially at a location away from the shear layers following the bulk flow, so it describes the most stable component. If another vertical location is selected closer to the lower wall (figure 11*b*, $y = -0.48$) a completely different pattern is produced suggestive of strong variation in the spanwise direction. In fact, some of the streamlines follow a closed-loop trajectory that forms the recirculating zone at certain spanwise locations, while the rest are subjected to strong modulation as they propagate downstream. A more illustrative pattern of streamlines is shown in figure 11(*c*) corresponding to a starting location at $y = -0.52$ inside the separation zone; again not all streamlines form closed-loop shapes. On the upper wall, where two-dimensional simulations reveal the existence of a secondary recirculation zone the picture is very similar; in figure 11(*d*)

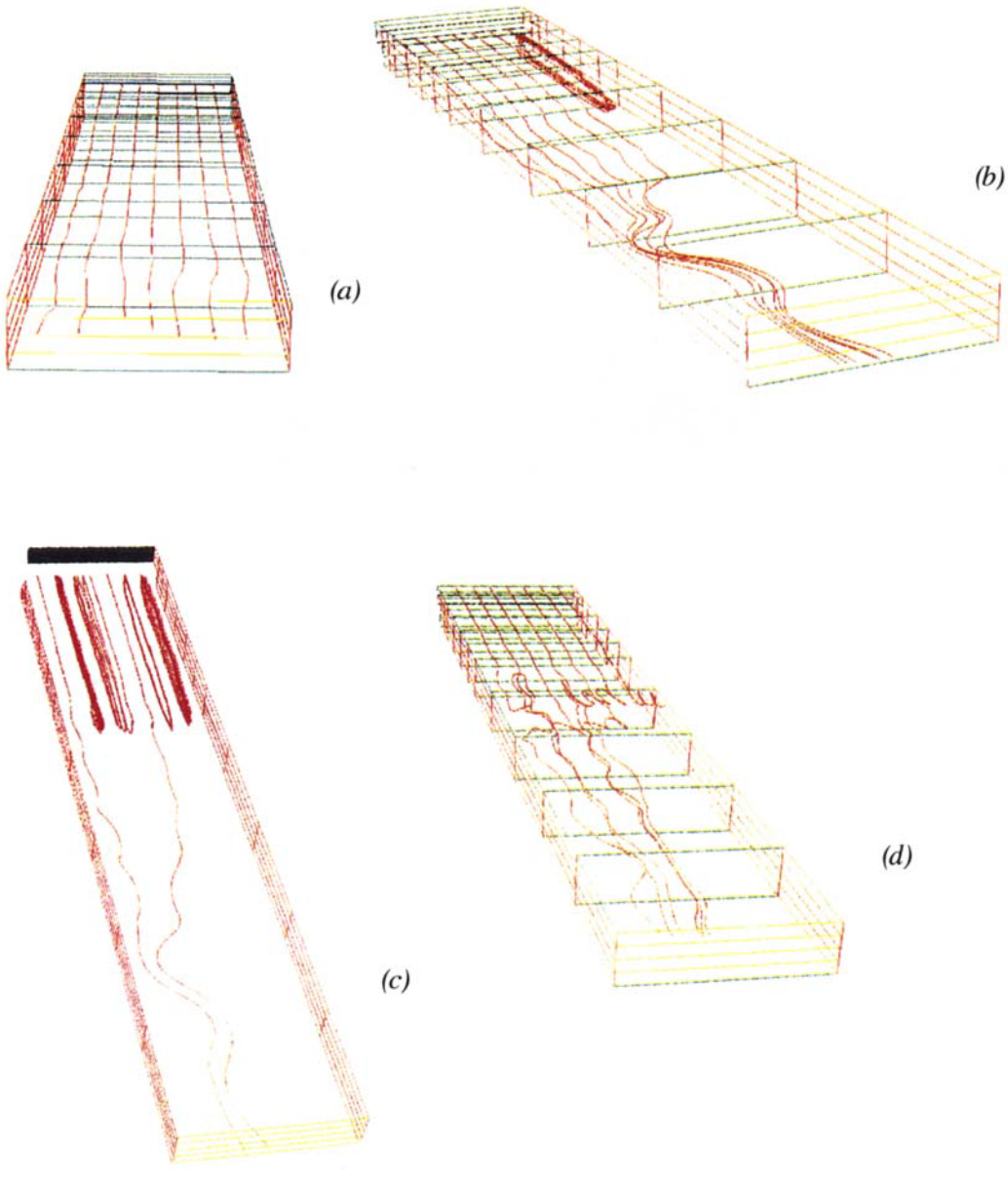

FIGURE 11. Families of instantaneous three-dimensional streamlines emanating from different y-locations (Re=800): (*a*) y=0, (*b*) y=−0.48, (*c*) y=−0.52, (*d*) y=0.45.

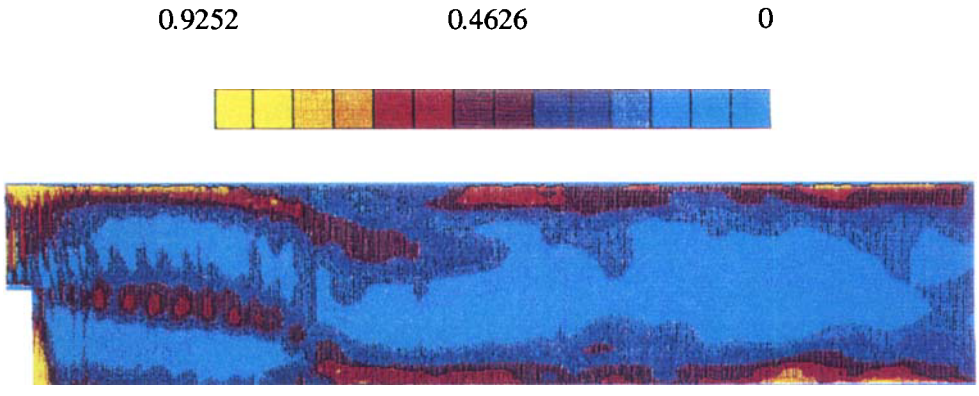

FIGURE 17. Colour-coded contours of the time-average spanwise anisotropy index $\overline{\eta}_1(x,y)$ at $Re=800$.

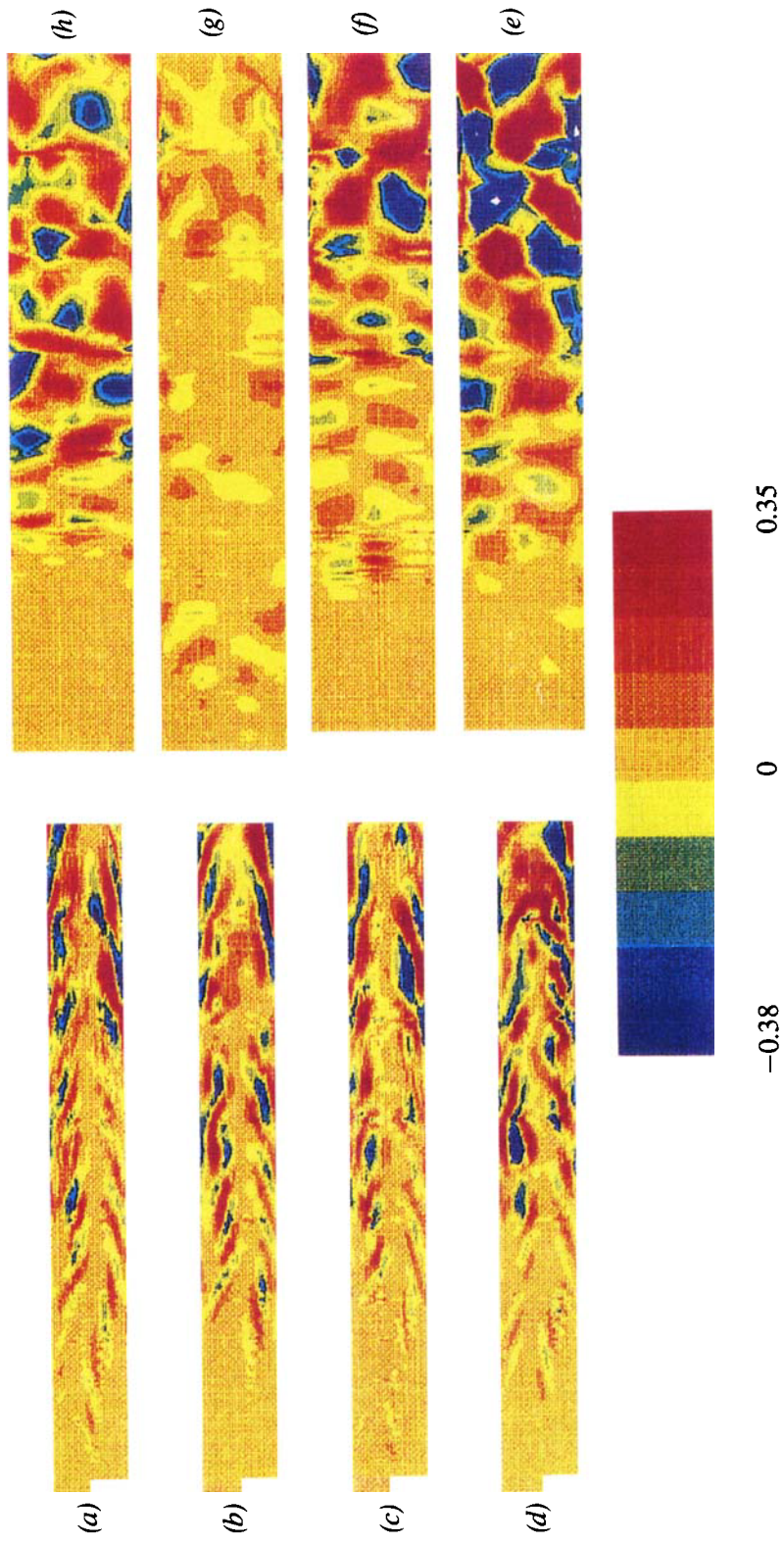

FIGURE 24. Streamwise vorticity colour-coded contours at different z- and y-planes. (*a*) $z=0$, (*b*) $z=\frac{1}{3}\pi$, (*c*) $z=\pi$, (*d*) $z=\frac{5}{3}\pi$, (*e*) $y=-1.44$, (*f*) $y=-0.75$, (*g*) $y=-0.4$, (*h*) $y=0.4$.

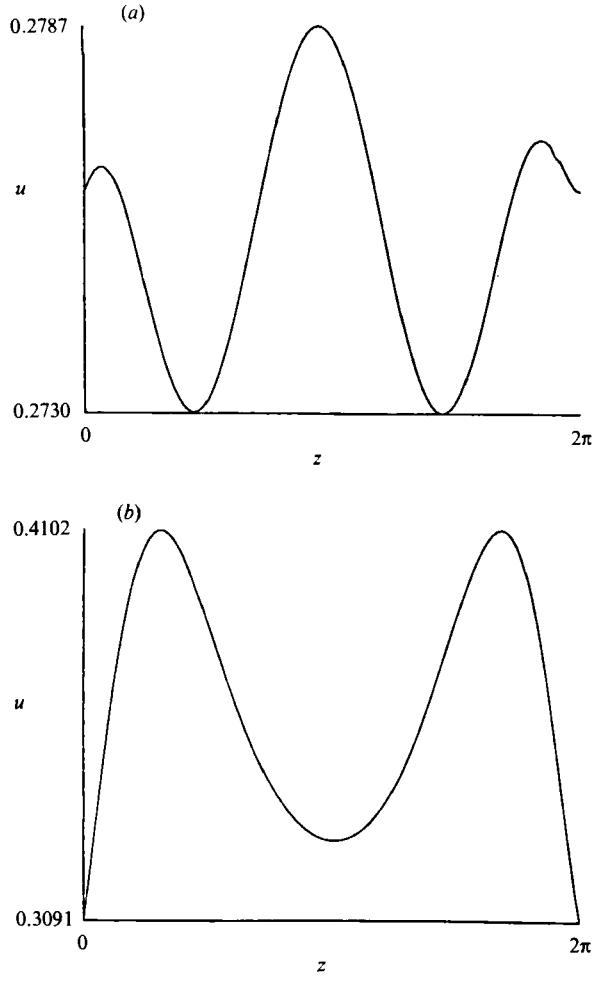

FIGURE 13. Time-average streamwise velocity distribution along the spanwise direction z ($Re = 800$): (*a*) $x = 6.0$, $y = -0.6$; (*b*) $x = 27.5$, $y = 0$.

streamlines emanating from $y = 0.45$ (very close to the upper wall) show a strong modulation, which is initiated at the region of the secondary bubble and persists downstream.

As in the two-dimensional simulations, the flow is quasi-periodic at $Re = 800$. In figures 12(*a*) and 12(*b*) we plot the power spectra of streamwise components at points P_1 and P_2 (similar to plots in figure 6 for the two-dimensional simulation). The co-existence of two incommensurate frequencies in the system is responsible for the quasi-periodicity; in fact, the frequency f_1 corresponding to two-dimensional T–S waves remains the same, while the upstream frequency f_2 is reduced by 10%. This shift of frequency is therefore associated with the three-dimensionality of the flow, the effects of which are apparently more pronounced in the upstream inflexional region.

The instantaneous variation in the spanwise direction produces a modulated time-average flow through nonlinearity. The amplitude of this modulation varies from location to location as seen in figures 13(*a*) and 13(*b*) in which streamwise profiles are plotted at an upstream station ($x = 6.0$) and a downstream station ($x = 27.5$) at

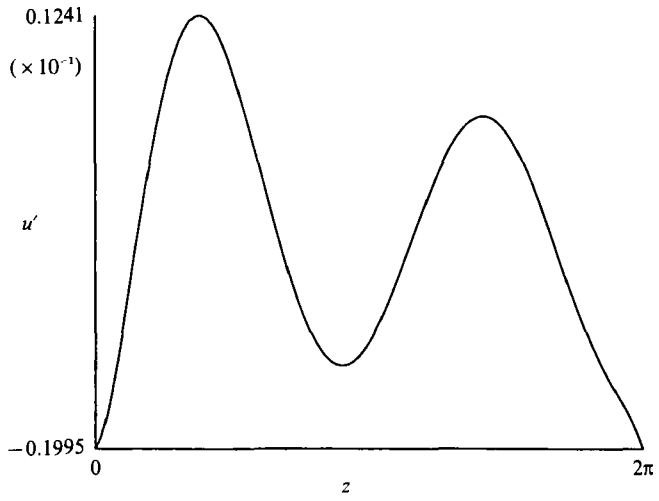

FIGURE 14. Streamwise component of the fluctuating velocity $u' = u - \bar{u}$ as a function of z at $x = 6.0$, $y = -0.6$ ($Re = 800$).

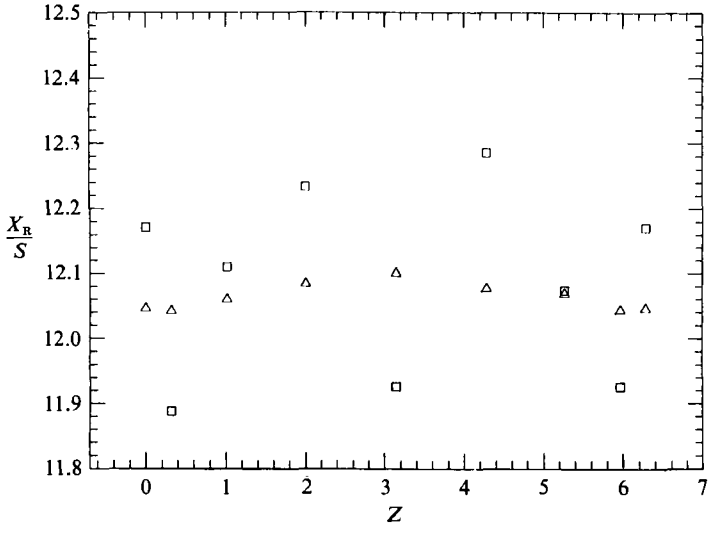

FIGURE 15. Time-averaged normalized recirculation length (X_R/S) versus spanwise distance z: △, $Re = 800$; □, $Re = 1095$.

$Re = 800$. The modulation is significantly stronger at $Re = 1095$, which is well above criticality. The fact that the wavelength of the modulated pattern is substantially smaller than the spanwise size of the domain is an indication that the selected pattern corresponds to the most unstable mode resolved by the simulation and thus is not affected by the periodic domain. An interesting feature of the spanwise structure recently discovered in three-dimensional wake flows (Karniadakis & Triantafyllou 1991) is the relation between the wavelength $\bar{\lambda}$ of the time-average streamwise flow velocity and its fluctuating counterpart λ': linear theory arguments and direct simulations suggest that $2\bar{\lambda} = \lambda'$, at least for slightly supercritical

Reynolds number. This spatial structure is not present, however, in the flow over a step (see the fluctuation profile plotted in figure 14) as the separated flow upstream corresponds to a convectively unstable pattern (compared to absolutely unstable modes in wake flows).

To assess the effect of the spanwise modulation in the location of primary and secondary separation bubbles, we next plot X_R/S along the z-direction for $Re = 800$ and 1095; in figure 15 the time-average values for both cases are shown. For $Re = 800$ the equivalent two-dimensional field $\langle \bar{v} \rangle$, obtained by averaging in z and time (see notation in §4), gives a value of X_R/S which differs by less than 1% from the one obtained by a purely two-dimensional computation. For $Re = 1095$, $\langle \bar{v} \rangle$ gives an increase in X_R/S of 6.6%.

4. Spanwise variation

In this Section, we address the question of the onset of three-dimensionality. The mean flow field varies in the x-direction, so global indices should be introduced that measure three-dimensionality and more general features of inhomogeneity in the spanwise direction. The key idea here is to associate the actual three-dimensional time-dependent field to an equivalent two-dimensional field at the same Reynolds number. This equivalent field is constructed from the results of the three-dimensional simulation by averaging instantaneous fields along the spanwise direction and in time. The streamline pattern of such an equivalent two-dimensional flow field at $Re = 800$ is plotted in figure 16.

Spanwise flow variation can be quantified through the use of several indices. First, there is the time-dependent inhomogeneity index η_1 (suggested to us by Dr Z. S. She)

$$\eta_1(x,y,t) = \frac{\langle (w - \langle w \rangle)^2 \rangle}{\langle (u - \langle u \rangle)^2 + (v - \langle v \rangle)^2 + (w - \langle w \rangle)^2 \rangle}, \tag{2a}$$

where $\langle\ \rangle$ denotes averaging in the spanwise direction. This index is a relative measure of the non-uniformity of the w-velocity component in the spanwise direction compared to the non-uniformity of all three components. The definition of η_1 assumes that the flow is fully three-dimensional; for two-dimensional regions both the numerator and denominator are zero so this index becomes meaningless. A more appropriate index for quantifying the onset of three-dimensionality is given by

$$\eta_2(x,y,t) = \frac{\langle (u')^2 + (v')^2 + (w')^2 \rangle}{(u'')^2 + (v'')^2 + (w'')^2}, \tag{2b}$$

where the three-dimensional fluctuating quantities are defined as $u' = u - \langle u \rangle$, while the two-dimensional ones are defined as $u'' = \langle u \rangle - \langle \bar{u} \rangle$ (here the overbar denotes time average), and similarly for the other components. According to this definition, two-dimensional unsteady states correspond to $\eta_2 = 0$, while the definition of η_2 breaks down for steady two-dimensional laminar states. These latter states can be identified by a third three-dimensionality index defined directly from the instantaneous velocity components as

$$\eta_3(x,y,t) = \frac{\langle w^2 \rangle}{\langle u^2 + v^2 + w^2 \rangle}. \tag{2c}$$

Steady two-dimensional states are then characterized by $\eta_3 = 0$. All three indices

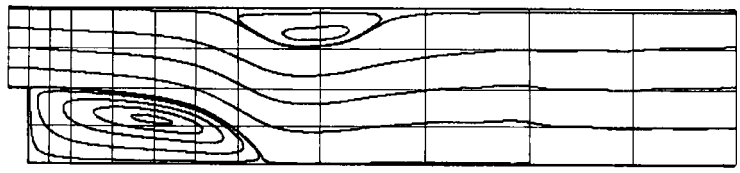

FIGURE 16. Streamline pattern of the equivalent two-dimensional velocity field $\langle \bar{v} \rangle$ at $Re = 800$. Here $\langle\ \rangle$ indicates spanwise average.

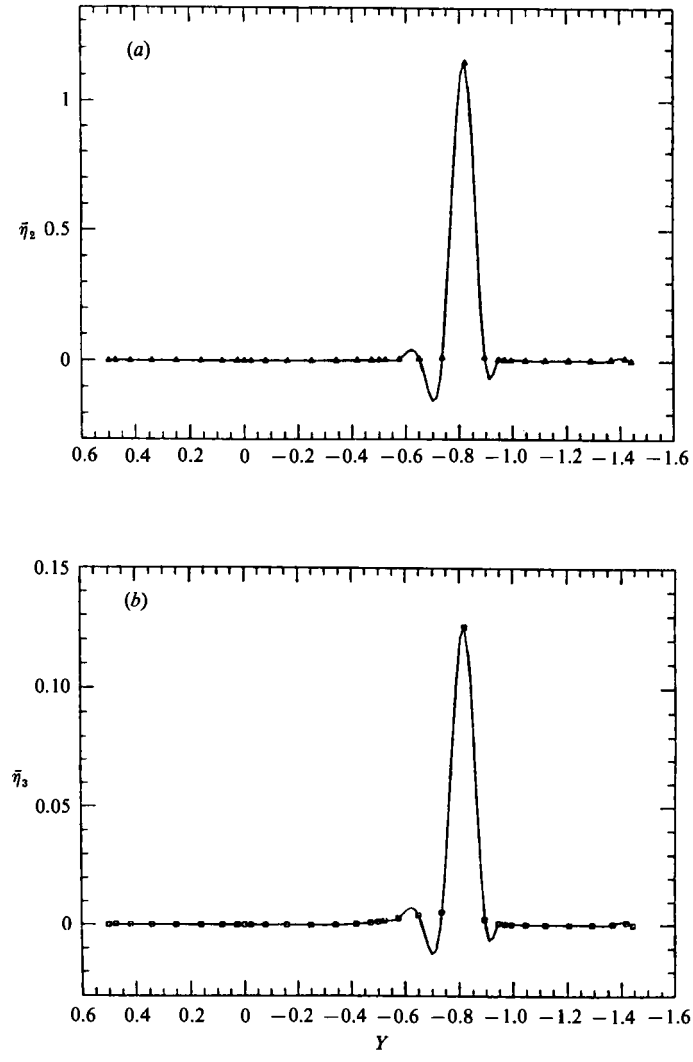

FIGURE 18. Three-dimensionality indices $\bar{\eta}_2, \bar{\eta}_3$ versus y at $Re = 800$: (a) $\bar{\eta}_2(x = 5.0; y)$, (b) $\bar{\eta}_3(x = 5.0; y)$.

defined in (2) are needed as they all assess three-dimensionality and inhomogeneity in different flow states.

A global picture of variation in the z-direction can be constructed based on the time-average values $\bar{\eta}_1(x, y)$ as shown in figure 17 (plate 2). A careful comparison of

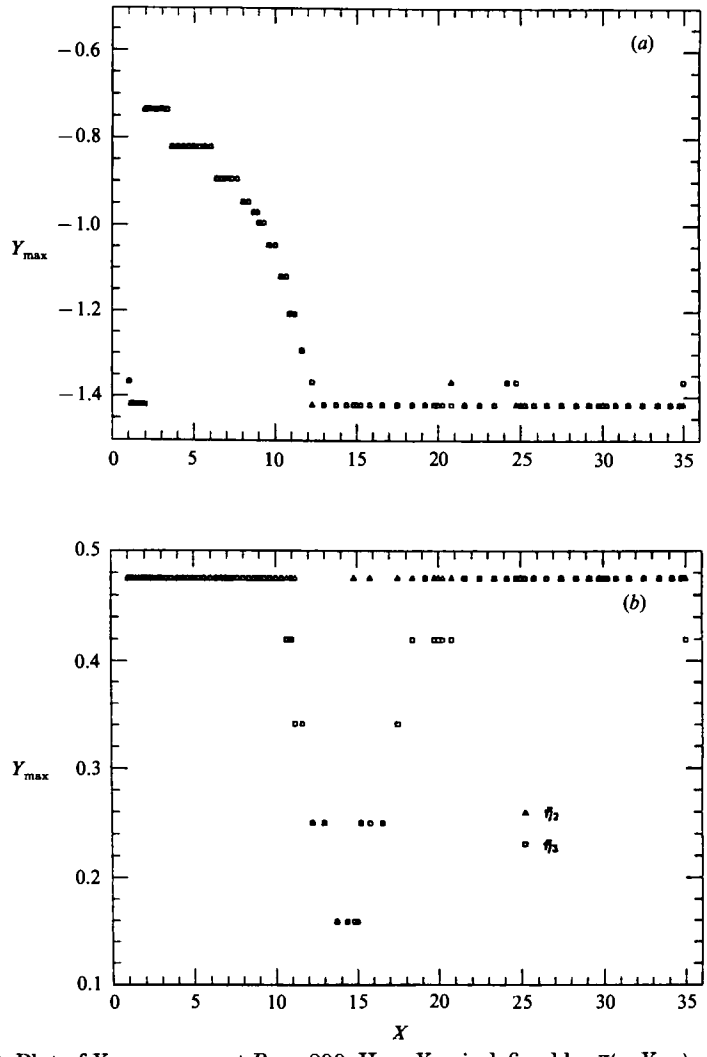

FIGURE 19. Plot of Y_{max} across x at $Re = 800$. Here Y_{max} is defined by $\bar{\eta}(x, Y_{max}) = \max \bar{\eta}(y)$ for a fixed x and y varying inside the region S. Here S is a subdomain of the step geometry. △, $\bar{\eta}_2$; □, $\bar{\eta}_3$. (*a*) Lower wall region: S is the domain S_l for $y \leqslant -0.2$; (*b*) upper wall region: S is the domain S_u for $y \geqslant -0.2$.

the equivalent spanwise-averaged field (figure 16) and this plot suggests that there exists a remarkable relation between the average $\bar{\eta}_1$ map and the flow field: high values of $\bar{\eta}_1$ are observed at the boundaries of the two separation zones and the bulk of the flow, the latter being the most stable component. It is thus concluded that three-dimensionality is initiated in those regions. High values of the index are also observed downstream along the extension of the shear layers passing through these highly three-dimensional regions. The unphysical high values of the index right at the inflow are an artifact as the definition of η_1 breaks down in purely two-dimensional states. The above results on the onset of three-dimensionality are also verified if the time-average indices $\bar{\eta}_2, \bar{\eta}_3$ are employed. More quantitatively, profiles of these latter indices are shown in figure 18 (*a*, *b*) at a characteristic location through the primary separation zone ($x = 5.0$). Both $\bar{\eta}_2$ and $\bar{\eta}_3$ peak at exactly the same

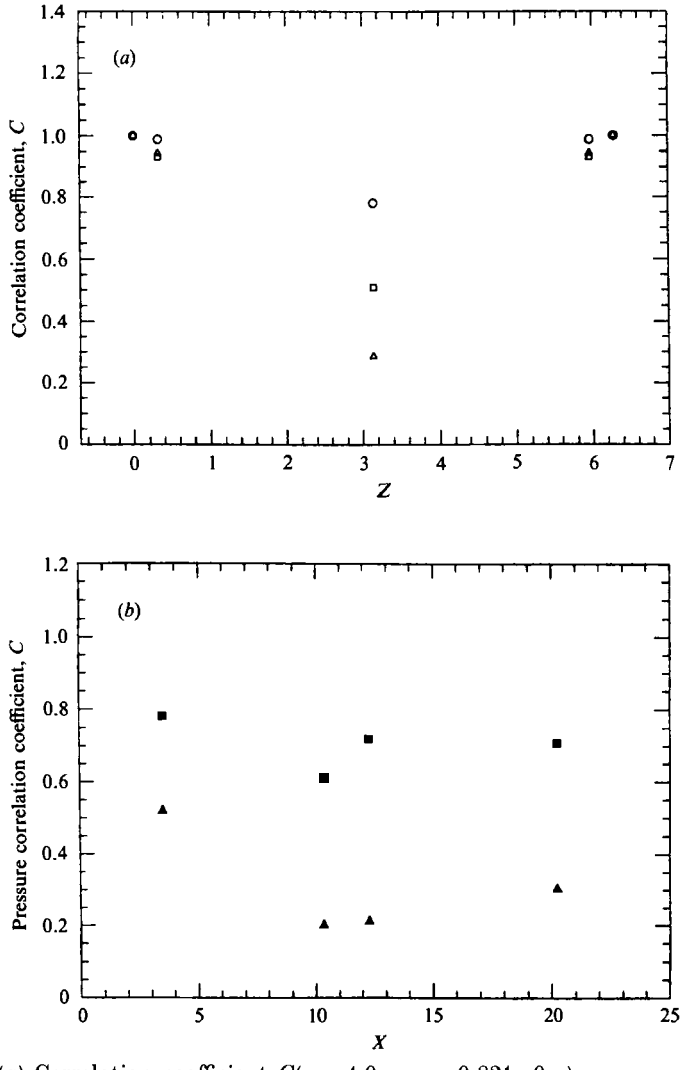

FIGURE 20. (*a*) Correlation coefficient $C(x = 4.0,\ y = -0.821;\ 0, z)$ versus spanwise separation z at $Re = 800$: ○, pressure; □, u-velocity; △, v-velocity. (*b*) Pressure correlation coefficient $C(x, y; 0, \pi)$ for the flows at $Re = 800$ (■), and 1095 (▲). Here (x, y) are the coordinates of the points Q_i, $(i = 1, \ldots, 4)$ defined in the text.

(x, y)-point. At another characteristic position through the reattachment point, the maxima of $\bar{\eta}_3$ are very close to the lower and upper walls within the shear layers formed at the boundaries of the two separation bubbles. Further downstream, all indices follow the spatial evolution described in figure 17.

Since there are clearly two distinct regions where onset of three-dimensionality occurs, namely the region S_l in the lower half of the domain and the region S_u in the upper part of the domain, it is appropriate that we examine them separately. Taking the lower part first we plot in figure 19(*a*) the (x, y)-position of the maxima of $\bar{\eta}_2$ and $\bar{\eta}_3$. A similar plot can be constructed for the upper region S_u (see figure 19*b*). It is clear from these figures that all indices we have introduced here are very sharp measures of three-dimensionality, and provide a consistent global picture of the spatial evolution of the three-dimensional instability.

A standard way to identify spanwise variation is through two-point correlations of a quantity computed at the same (x, y)-point and different z-locations. The corresponding spanwise correlation coefficient is defined as

$$C(x, y; z_i, z_j) = \frac{\overline{q_i q_j}}{(\overline{q_i^2}\,\overline{q_j^2})^{\frac{1}{2}}}, \tag{3}$$

where q_i and q_j denote fluctuations in time of the quantity at points (x, y, z_i), (x, y, z_j), and the overbar indicates time averaging as before. Here we trace all field quantities at four characteristic (x, y)-locations: inside the recirculation zone $Q_1 \equiv (x_1 = 4.0, y_1 = -0.821)$, upstream in the shear layer $Q_2 \equiv (x_2 = 10.4, y_2 = -0.650)$, above the reattachment point $Q_3 \equiv (x_3 = 12.3, y_3 = -0.821)$, and at a point further downstream at $Q_4(x_4 = 20.3, y_4 = -0.821)$. Four different z-locations were examined: $z = 0$, $0.05L_z$, $0.5L_z$, and $0.95L_z$. A typical result for the correlation coefficient $C(x_1, y_1; 0, z)$ at the location (x_1, y_1) (at $Re = 800$) is shown in figure 20 (*a*). The general conclusion is that the pressure exhibits a higher spanwise correlation than the velocity field. The magnitude of three-dimensionality is indicated by examining the correlation of pressure at the fixed spanwise separation $z = 0.5L_z$ (see figure 20*b*). The rapid decrease in this correlation in the reattachment zone as the Reynolds number increases is consistent with the scenario of abrupt transition proposed earlier. Conclusively, high correlation is obtained in the innermost part of the recirculating zone and in the bulk of the flow downstream, while lower correlations are obtained at the shear layer and in the region above the reattachment point.

5. Non-ideal flow conditions

5.1. *External excitation*

In this Section, we report results of a forced experiment simulating the flow over a backward-facing step, where the inflow boundary condition is modified to include small-amplitude time-periodic excitations superimposed on the parabolic basic profile. In particular, the flow is excited at its two fundamental frequencies f_1 and f_2 as well as at two incommensurate frequencies $f_1^* = gf_1$ (where $g = 0.618\ldots$ is one half of the golden ratio), and $f_2^* = 0.565$. We perform two sets of experiments with the amplitude of the excitation at $\epsilon = 0.01$ and $\epsilon = 0.05$, respectively. The objective of the forced experiment is twofold: first, to verify that the two frequencies f_1 and f_2 present at $Re = 800$ are the two fundamental frequencies of the flow corresponding to the channel flow and the upstream shear layer respectively; and secondly, to assess the effect of free disturbances (unavoidable in a laboratory experiment) on transition, and in particular on such readily observed measures as the time-average size of the two separation zones.

Past experience suggests that even small-amplitude excitation can completely alter the pattern of a flow especially in the presence of separation, which increases the receptivity region (Ghaddar *et al.* 1986; Karniadakis & Triantafyllou 1989). The most dramatic response typically occurs at resonant conditions, at which the flow locks-in to a single frequency state if the excitation amplitude exceeds a (small) threshold amplitude. To test these ideas we first perform a two-dimensional simulation at $Re = 800$, imposing an excitation of amplitude $\epsilon = 0.01$ and frequency $f_e = f_1$. It is seen from the time spectra plotted in figure 21 (*a*) (at point P_2) that although the dominant frequency of the response is the excitation frequency, the shear-layer frequency is still present. In fact, this forcing results in a more precisely defined quasi-periodic oscillatory state. Repeating the experiment at higher

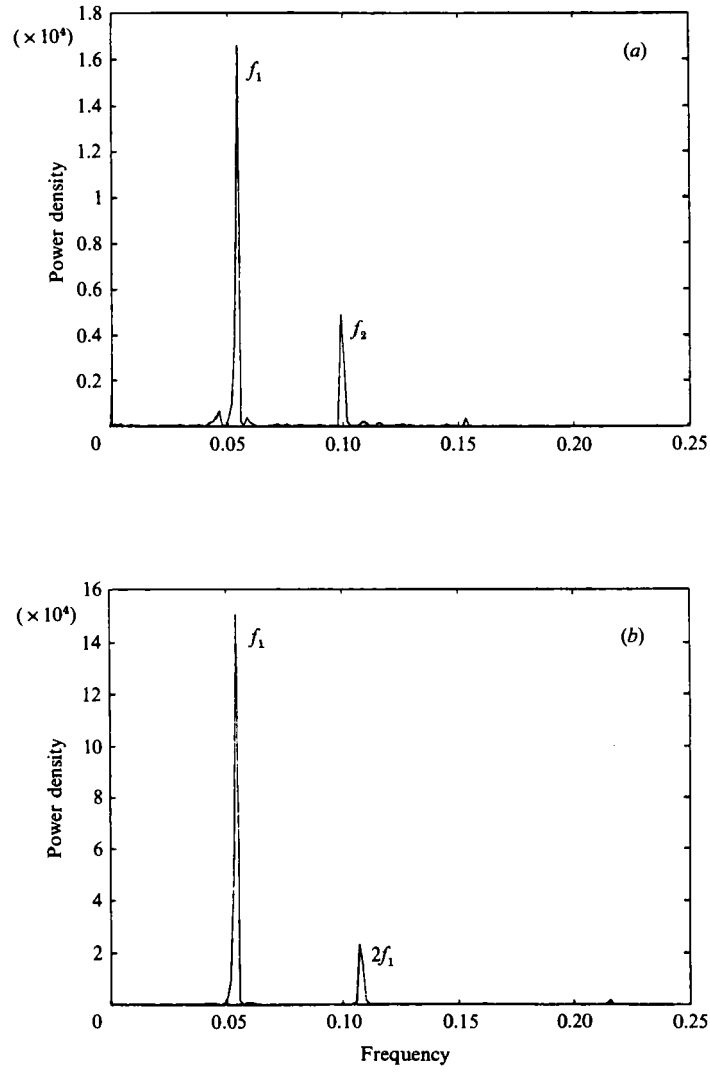

FIGURE 21. Power spectra in time at point P_2 for the forced flow of frequency f_e at $Re = 800$. (*a*) $\epsilon = 0.01$; $f_e = f_1$. (*b*) $\epsilon = 0.05$; $f_e = f_1$.

amplitude $\epsilon = 0.05$ the flow locks-in to a single frequency state as shown in figure 21 (*b*), where the second natural frequency has completely disappeared, giving rise to superharmonics. The corresponding change in X_R is now very different than previously, since X_R decreases by 17%. This is of course intuitively correct; at the lock-in state the enhanced Reynolds stresses due to resonant excitation produce an increased apparent viscosity that reduces the size of the separation region.

Repeating the latter experiment at the second natural frequency f_2 and amplitude $\epsilon = 0.05$ a lock-in state is established that corresponds to a further decrease in $X_R/S = 9.25$, a decrease of 24% as compared to the corresponding value of the unforced case. If the flow is disturbed at an incommensurate frequency f_1^* as described above, a three-period state (at the low amplitude $\epsilon = 0.01$) or a lock-in state (at the higher amplitude $\epsilon = 0.05$) can result, which lead to an increase in X_R by 2.2 and 0.9%, respectively. So far, these results indicate that low-amplitude

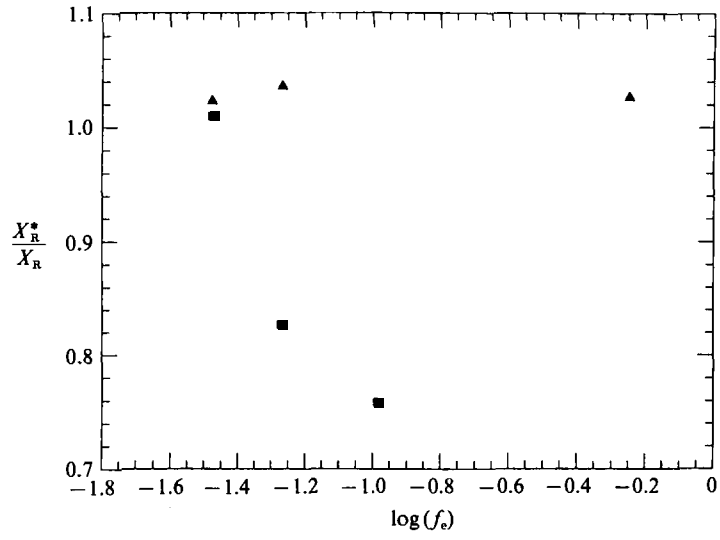

FIGURE 22. Ratio of recirculation length (X_R^*/X_R) of the forced and unforced flows at $Re = 800$ as a function of the forcing frequency f_e. ▲, $\epsilon = 0.01$; ■, $\epsilon = 0.05$.

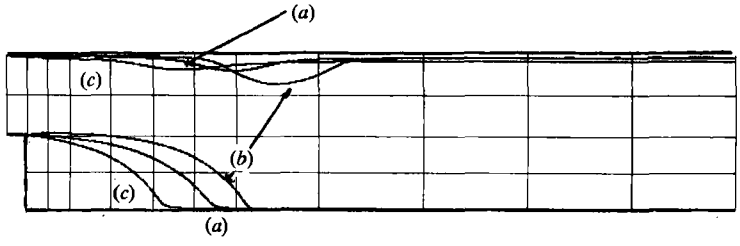

FIGURE 23. Dividing streamlines for different inflow profiles ($Re = 500$): (*a*) parabolic profile, (*b*) triangular profile, (*c*) uniform profile.

excitations lead to an increase in X_R. This can be attributed to the fact that the time-average momentum influx is increased, with no significant changes in the Reynolds stress distribution. To further confirm this assumption, we perform an experiment at a higher frequency $f_2^* = 0.565$; in this case an increase is obtained again in X_R, by 2.6%. The results of the above experiment are summarized in figure 22; it is seen that even the 1% excitation can lead to approximately a 5% increase or decrease in the separation length X_R, which reflects the wide receptivity region of separated flows.

5.2. *Inflow mean profiles*

In spatially developing flows the velocity distribution of the incoming flow can greatly alter the transition process. In this Section, we examine this effect of the inflow velocity profile in a manner similar to the last Section. In particular, we consider two non-parabolic inflow distributions and compare the results to our standard parabolic inflow case studied in detail here. In all cases, the mass flow rate is kept constant equal to $Q = \frac{2}{3}$ non-dimensional units; the kinematic viscosity is also kept constant. For the standard parabolic profile case, these experiments correspond to $Re = 500$ (see figure 3).

The additional profiles considered are a symmetric triangular profile and an almost uniform (blunt-like) profile; these profiles are fully specified by the requirement that $Q = \frac{2}{3}$. The results of the simulation reveal significant changes in the flow pattern,

most readily observed by comparing the relative size of the primary and secondary recirculating zones. This is graphically illustrated in figure 23, where the separation streamlines are plotted for the lower and upper wall for all three cases. In more quantitative form, the triangular inlet profile produces a recirculation length X_R which is 18.4% longer than the parabolic inlet profile case. In the case of a blunt inflow profile, however, the value of X_R is decreased by 26.9%. The position as well as the size of the secondary bubble in the upper wall is similarly affected.

5.3. *Effect of sidewalls*

To further explore other possible influences on the flow structure, the geometry (see figure 2) was modified at the sides so that solid (no-slip) walls replaced the periodic conditions. All simulations in this case were run at $Re = 800$, with a parabolic profile imposed at inflow. The distribution of (Gauss–Lobatto–Legendre) collocation points (9 and 12 for two different calculations) is such that higher resolution is placed closer to the sidewalls. The spanwise distance was kept the same, $L_z = 2\pi$, although the distance between the sidewalls in the physical experiment (Armaly *et al.* 1983) is more than seven times our L_z; however, the resolution requirements for this laboratory experiment by far exceed the computational resources available at the present time. The results of our simulation indicate that, as a function of spanwise location, the recirculation length X_R peaks midway between the sidewalls, with the average value at the centreline being approximately 4% shorter than the corresponding X_R of the periodic case.

6. Discussion

In this paper, we have investigated numerically the onset of three-dimensionality and resulting flow states in the early transitional regime for flow over a backward-facing step. Our results suggest that the steady laminar flow bifurcates to a three-dimensional oscillatory state the first time the flow loses stability, implying that a secondary instability develops at essentially the same critical Reynolds number Re_c as the primary bifurcation. This finding is based on extensive numerical experimentation with different forms of external excitation (see Kaiktsis 1990); a more detailed study requires a multi-dimensional numerical bifurcation analysis and prohibitively expensive computations. In effect, therefore, all unsteady states of the flow are three-dimensional and develop for Reynolds number $Re \geqslant Re_c \approx 700$. Onset of three-dimensionality occurs in specific regions of the flow determined by the separation regions, and, in particular, at the boundaries between the two separated stagnant flow zones and the bulk of the flow. This idea has been quantitatively verified through standard spanwise correlation coefficients and also by three different types of inhomogeneity indices η_1, η_2, η_3 introduced in this work.

The resulting three-dimensional states are 'stable' at finite amplitudes. Slightly supercritical states ($Re > 700$) are periodic with the shear-layer frequency f_2 dominating everywhere in the field. At Reynolds number $Re > 800$ quasi-periodic states are formed which are characterized by two frequencies f_1 and f_2 that reflect the basic structure of the flow, namely the channel parabolic flow downstream and the shear layer upstream, respectively. An eigenvalue analysis reveals a close resemblance of the fluctuating velocity field downstream with channel Tollmien–Schlichting (T–S) waves, typically encountered at higher Reynolds number. The presence of an unstable shear layer upstream, however, causes excitation of these 'native' T–S waves even at strongly subcritical Reynolds numbers (i.e. $Re = 800$).

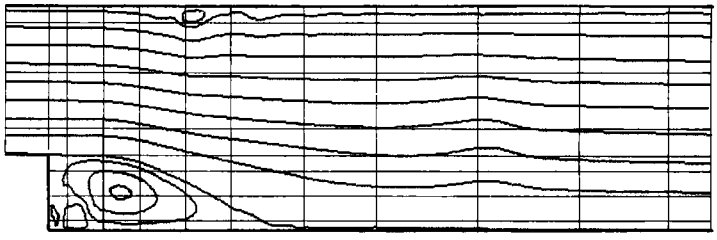

FIGURE 25. Streamlines of the mean flow at $Re = 45000$.

The exact nature of the breaking of the quasi-periodic states as Re increases has not yet been determined. However, power spectra in time at $Re = 1095$ show a much richer frequency content. Careful examination of frequency spectra at $Re = 800$ at sixteen different locations reveals a continuous shift of the maximum power spectral density from f_1 and f_2 from location to location. In fact, at certain locations the spectral density peaks either at a superharmonic $2f_1$ or at a subharmonic $\frac{1}{2}f_2$. The corresponding pairs $(2f_1, f_2)$, or $(f_1, \frac{1}{2}f_2)$, therefore, have very close values. According to the theory proposed by Karniadakis & Triantafyllou (1989) quasi-periodicity, lock-in states, or weakly chaotic states are possible, depending on threshold amplitude. This 'pattern competition scenario' to chaos, first put forward by Ciliberto & Gollub (1984), may be applicable here as a possible alternative to the RTN scenario (Newhouse, Ruelle & Takens 1978) postulated for quasi-periodic flows. This issue however should be further investigated in future work.

Although the backward-facing step geometry considered here is two-dimensional, the time-average flow acquires a modulated spanwise structure. This result is a fundamental difference from simple-geometry non-inflexional flows (e.g. plane Poiseuille flow), where the mean flow varies only in the direction normal to the walls. Recent studies on three-dimensional wakes formed behind two-dimensional cylinders (Karniadakis & Triantafyllou 1991) suggest that in this case the mean flow also varies in all three dimensions. This three-dimensionality in the mean produces a streamwise vorticity distribution with a rib-like structure similar to the one observed in compressible planar wakes (Chen, Cantwell & Mansour 1989). In figure 24 (plate 3) we plot streamwise vorticity contours at $Re = 800$ for different spanwise (*a–d*) and horizontal (*e–h*) planes; vorticity streaks emanating from the two walls are clearly shown in the side views (notice that the scale is highly compressed in the streamwise direction for plotting purposes). The plane corresponding to $y = -1.44231$ coincides with the lower wall and hence the large magnitude of vorticity; in contrast, small variations are shown in the bulk of the flow ($y = -0.4$).

The flow over a backward-facing step with expansion ratio $r \approx 2$ becomes turbulent at $Re = 5000$ according to the experimental results of Armaly *et al.* (1983). Recent work using spectral-element discretizations combined with renormalization group techniques (Yakhot & Orszag 1986; Karniadakis *et al.* 1989) in fact predicts transition to turbulence at approximately the same Reynolds number. At high Reynolds number the flow acquires a different structure, characterized by a shorter primary separation zone as well as the appearance of a multi-eddy structure at the junction of the vertical and lower wall inside. This latter feature has been observed experimentally by Tani, Inchi & Komoda (1967) and simulated using spectral element–renormalization group technique computations at $Re = 45000$ (see figure 25; Karniadakis *et al.* 1989). Simulations for the geometry considered here at $Re = 4444$ indicate that the multi-eddy structure is also a feature of the late tran-

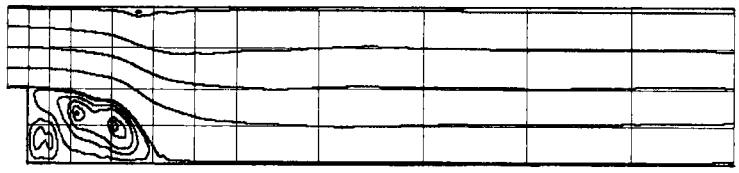

FIGURE 26. Streamline pattern of the equivalent two-dimensional velocity field $\langle \bar{v} \rangle$ at $Re = 4444$.

sitional regime. This is demonstrated in figure 26, where we plot the equivalent two-dimensional velocity field $\langle \bar{v}(x) \rangle$ in the form of streamlines. In work still underway we are studying the flow structure at these Reynolds numbers in the late transitional and early turbulent regime using both direct and large-eddy simulations based on renormalization subgrid modelling techniques. These results will be reported later.

Financial support for the current work was provided by grants from the NSF (CTS-8906911 and CTS-8906432) and by ONR Contract N00014-82-C-0451. Most of the computations were performed on the Cray-Y/MP at the Pittsburgh Supercomputing Center, and at the Numerical Aerodynamic Simulation Facility at NASA Ames.

Appendix

A 1. *Semi-discrete formulation*

The time-discretization employs a high-order splitting algorithm based on mixed stiffly stable schemes (Karniadakis, Israeli & Orszag 1991). Considering first the nonlinear terms we obtain

$$\frac{\hat{v} - \sum_{q=0}^{J-1} \alpha_q v^{n-q}}{\Delta t} = \sum_{q=0}^{J-1} \beta_q [-N(v^{n-q})], \tag{A 1a}$$

where $N(V^n) = \frac{1}{2}[v^n \cdot \nabla v^n + \nabla \cdot (v^n v^n)]$ represents the nonlinear contributions written in skew-symmetric form at time level $(n+1)\Delta t$, and α_q, β_q are implicit/explicit weight coefficients for the stiffly stable scheme of order J (see Karniadakis *et al.* 1991). The next substep incorporates the pressure equation and enforces the incompressibility constraint as follows:

$$\frac{\hat{\hat{v}} - \hat{v}}{\Delta t} = -\nabla p^{n+1}, \quad \nabla \cdot \hat{\hat{v}} = 0. \tag{A 1b, c}$$

Finally, the last substep includes the viscous corrections and imposes the boundary conditions, i.e.

$$\frac{\gamma_0 v^{n+1} - \hat{\hat{v}}}{\Delta t} = Re^{-1} \nabla^2 v^{n+1}, \tag{A 1d}$$

where γ_0 is a weight coefficient of the backwards differentiation scheme employed (Karniadakis *et al.* 1991).

The above time treatment of the system of equations (1) results in a very efficient calculation procedure as it decouples the pressure and velocity equations as in

(A 1*b*, *c*) and (A 1*d*). High-order time accuracy of this splitting scheme is achieved by solving the pressure equation (A 1*b*, *c*) in the form

$$\nabla^2 p^{n+1} = \nabla \cdot \left(\frac{\hat{v}}{\Delta t} \right) \tag{A 2}$$

along with the consistent high-order pressure boundary condition (see Karniadakis *et al.* 1991)

$$\frac{\partial p^{n+1}}{\partial n} = \boldsymbol{n} \cdot \left[-\sum_{q=0}^{J-1} \beta_q N(\boldsymbol{v}^{n-q}) - Re^{-1} \sum_{q=0}^{J-1} \beta_q [\nabla \times (\nabla \times \boldsymbol{v}^{n-q})] \right], \tag{A 3}$$

where $\boldsymbol{n}$ denotes the unit normal to the boundary Γ. Equation (A 2) is a Poisson equation with constant coefficients, which can be rewritten in the standard form

$$\nabla^2 \phi = g(\boldsymbol{x}), \tag{A 4}$$

where we have defined $\phi = p^{n+1}$, and $g(\boldsymbol{x}) \nabla \cdot (\hat{v}/\Delta t)$. In the following § A 2 we will refer to this equation in order to discuss the spatial discretization of (A 1) using the spectral-element method.

A 2. *Spectral-element methodology*

The spatial discretization of (A 4) is obtained using the spectral-element methodology (Patera 1984; Karniadakis, Bullister & Patera 1985; Maday & Patera 1987; Karniadakis 1989, 1990). For a nominally two-dimensional geometry two different approaches can be followed. First, Fourier expansions can be used to represent data and field variables along the spanwise (homogeneous) direction; the problem is then reduced to solving M two-dimensional problems each time step (here M is the number of Fourier modes); the only coupling in z is through the nonlinear terms, where fast Fourier transforms can efficiently be used (see Karniadakis 1990). The second formulation is more general and can accommodate non-periodic boundary conditions. In particular, a general (Legendre) spectral expansion can be employed in the spanwise direction, while two-dimensional spectral elements represent the geometry in all (x, y)-planes. The most general case of using general hexahedra has been treated in Karniadakis *et al.* (1985), and Maday & Patera (1987). In the standard spectral-element discretization the computational domain Γ_m or Ω is broken up into several quadrilaterals in two dimensions or general brick elements in three dimensions, which are mapped isoparametrically to canonical squares or cubes respectively. Field unknowns and data are then expressed as tensor products in terms of Legendre–Lagrangian interpolants. The final system of discrete equations is then obtained using a Galerkin variational statement.

To illustrate the spectral-element methodology in more detail, we consider the elliptic model equation (A 4). for simplicity we only present the two-dimensional spectral-element equations, as the Galerkin spectral formulation in the spanwise direction is given by Gottlieb & Orszag (1977). We assume in addition homogeneous boundary conditions $\phi = 0$ on Γ. Equation (A 4) can then be discretized using planar spectral elements in the plane x, y. If we define as H_0^1 the standard Sobolev space that contains functions which satisfy homogeneous boundary conditions, and introduce test functions $\psi \in H_0^1$, we can then write the equivalent variational statement of (A 4) as

$$\int_\Omega \frac{\partial \psi}{\partial x_j} \frac{\partial \phi}{\partial x_j} \mathrm{d}s = -\int_\Omega \psi g \, \mathrm{d}s. \tag{A 5}$$

The spectral-element discretization corresponds to numerical quadrature of the variational form (A 5) restricted to the space $X_h \subset H_0^1$. The discrete space X_h is defined in terms of the spectral-element discretization parameters (K, N_1, N_2), where K is the number of 'spectral elements', and N_1, N_2 are the degrees of piecewise high-order polynomials in the two directions respectively that fill the space X_h. By selecting appropriate Gauss–Lobatto points ξ_{pq}^k and corresponding weights $\rho_{pq} = \rho_p \rho_q$, equation (A 5) can be replaced by

$$\sum_{k=1}^{K} \sum_{p=0}^{N_1} \sum_{q=0}^{N_2} \rho_{pq} J_{pq}^k \left[\frac{\partial \psi}{\partial x_j} \frac{\partial \phi}{\partial x_j} \right]_{\xi_{pq}^k} = - \sum_{k=1}^{K} \sum_{p=0}^{N_1} \sum_{q=0}^{N_2} \rho_{pq} J_{pq}^k [\psi g]_{\xi_{pq}^k}. \tag{A 6}$$

Here J_{pq}^k is the Jacobian of the transformation from global to local coordinates $(x, y) \Rightarrow (r, s)$ for the two-dimensional element k. The Jacobian is easily calculated from the partial derivatives of the geometry transformation r_x, r_y, s_x, s_y. The next step in implementing (A 6) is the selection of a basis which reflects the structure of the piecewise-smooth space X_h. We choose an interpolant basis with components defined in terms of Legendre–Lagrangian interpolants, $h_i(r_j) = \delta_{ij}$. Here, r_j represents local coordinate and δ_{ij} is the Kronecker-delta symbol. It was shown by Patera (1984) and Ronquist (1988) that such a spectral-element implementation converges spectrally fast to the exact solution for a fixed number of elements K and $N_{1,2,3} \to \infty$, for smooth data and solution, even in non-rectilinear geometries.

Having selected the basis we can proceed to write the spectral-element approximation for ϕ^k, (or ψ^k) as follows:

$$\phi^k = \phi_{mn}^k h_m(r) h_n(s) \quad \forall \quad m, \quad n \in (0, \ldots, N_1), (0, \ldots, N_2), \tag{A 7a}$$

where ϕ_{mn}^k is the local nodal value of ϕ. The geometry is also represented using similar-type tensor products with same-order polynomial degree, i.e.

$$(x, y)^k = (x_{mn}^k, y_{mn}^k) h_m(r) h_n(s) \quad \forall \quad m, \quad n \in (0, \ldots, N_1), (0, \ldots, N_2). \tag{A 7b}$$

Here x_{mn}^k, y_{mn}^k are the global physical coordinates of the node mn in the k element. This isoparametric mapping leads to a compatible pressure formulation without the presence of spurious modes due to ellipticity of the pressure equation (Karniadakis 1989).

We now insert (A 7a, b) into (A 6) and choose test functions ψ_{mn}, which are non-vanishing at only one global node to arrive at the discrete matrix system. This procedure is straightforward; the final matrix system is,

$$\sum_{k=1}^{K'} \sum_{m=0}^{N_1} \sum_{m=0}^{N_2} (P_{ijmn}^{x,k} + P_{ijmn}^{y,k}) \phi_{mn}^k = - \sum_{k=1}^{K'} \sum_{m=0}^{N_1} \sum_{m=0}^{N_2} J_{ij}^k B_{im}^k B_{jn}^k g_{mn}^k, \tag{A 8a}$$

where $'$ denotes direct stiffness summation for the global system to ensure that the ensemble is performed in space H^1. The x-component, for example, of the Poisson operator is given by

$$P_{mn}^{x,k} = \rho_{pq} J_{pq}^k [(r_x)_{pq}^2 \, \mathrm{D}_{pi} \mathrm{D}_{pm} \delta_{nq} + (s_x)_{pq}^2 \, \mathrm{D}_{qj} \mathrm{D}_{qn} \delta_{mp} + (r_x s_x)_{pq} \mathrm{D}_{pi} \mathrm{D}_{qn} \delta_{mp} + (r_x s_x)_{pq} \mathrm{D}_{qj} \mathrm{D}_{pm} \delta_{nq}]. \tag{A 8b}$$

Here the derivative operator is defined as $\mathrm{D}_{ij} = \mathrm{d}h_j / \mathrm{d}z(\xi_i)$; all other parameters have been defined previously. The mass matrix B_{ij}^k is diagonal and is defined as $B_{ij}^k = \rho_i \delta_{ij}$. The y-component of the Poisson operator is defined similarly.

The natural choice of solution algorithm for (A 8a) is an iterative procedure; to date both conjugate gradient techniques and multigrid methods have been

implemented for elliptic equations (Ronquist 1988). The advantage of the formulation proposed here as compared to the formulation of Ronquist (1988) is that the high-order splitting scheme results in decoupled, elliptic equations for the pressure and velocity that can be very efficiently and robustly solved using those iterative techniques without the need of case-dependent preconditioners or other convergence acceleration techniques.

REFERENCES

ARMALY, B. F., DURST, F., PEREIRA, J. C. F. & SCHONUNG, B. 1983 Experimental and theoretical investigation of backward-facing step flow. *J. Fluid Mech.* **127**, 473.

AUNG, W. & GOLDSTEIN, R. J. 1972 Heat transfer in turbulent separated flow downstream of a rearward-facing step. *Israel J. Technol.* **20**, 35.

CHEN, J. H., CANTWELL, B. J. & MANSOUR, N. N. 1989 The topology and vorticity dynamics of a three-dimensional plane compressible wake. In *Proc. Tenth Austral. Fluid Mech. Conf., Melbourne, Australia* (ed. A. E. Perry).

CILIBERTO, S. & GOLLUB, J. P. 1984 Pattern competition leads to chaos. *Phys. Rev. Lett.* **52**, 922.

DENHAM, M. K. & PATRICK, M. A. 1974 Laminar flow over a downstream-facing step in a two-dimensional flow channel. *Trans. Inst. Chem. Engrs.* **52**, 361.

GHADDAR, N. K., KORCZAK, K. Z., MIKIC, B. B. & PATERA, A. T. 1986 Numerical investigation of incompressible flow in grooved channels. Part 1. Stability and self-sustained oscillations. *J. Fluid Mech.* **163**, 99.

GOTTLIEB, D. & ORSZAG, S. A. 1977 *Numerical Analysis of Spectral Methods: Theory and Applications.* Philadelphia: SIAM.

HERBERT, T. 1988 Secondary instability of boundary layers. *Ann. Rev. Fluid Mech.* **20**, 487.

KAIKTSIS, L. 1990 Three-dimensionality and stable equilibria in flow over a backward-facing step. Master's thesis, Dept. of Mechanical and Aerospace Engineering, Princeton University.

KARNIADAKIS, G. E. 1989 Spectral element simulations of laminar and turbulent flows in complex geometries. *Appl. Numer. Maths* **6**, 85.

KARNIADAKIS, G. E. 1990 Spectral element–Fourier methods for incompressible turbulent flows. *Comput. Math. Appl. Mech. Engng* **8**, 367.

KARNIADAKIS, G. E. & AMON, C. 1987 Stability calculations of wall-bounded flows in complex geometries. In *Proc. Sixth IMACS Symp. on PDEs*, p. 525.

KARNIADAKIS, G. E., BULLISTER, E. T. & PATERA, A. T. 1985 A spectral element method for solution of two- and three-dimensional time dependent Navier–Stokes equations. In *Proc. Europe–US Conf. on Finite Element Methods for Nonlinear Problems* (ed. P. G. Bergan, K. J. Bathe & W. Wunderlich), p. 803. Springer.

KARNIADAKIS, G. E., ISRAELI, M. & ORSZAG, S. A. 1991 High-order splitting methods for the incompressible Navier–Stokes equation. *J. Comput. Phys.* (to appear).

KARNIADAKIS, G. E., MIKIC, B. B. & PATERA, A. T. 1988 Minimum dissipation transport enhancement by flow destabilization: Reynolds' analogy revisited. *J. Fluid Mech.* **192**, 365.

KARNIADAKIS, G. E. & TRIANTAFYLLOU, G. S. 1989 Frequency selection and asymptotic states in laminar wakes. *J. Fluid Mech.* **199**, 441.

KARNIADAKIS, G. E. & TRIANTAFYLLOU, G. S. 1991 Three-dimensional bifurcation and transition to turbulence in the wake of bluff objects. *J. Fluid Mech.* (submitted).

KARNIADAKIS, G. E., YAKHOT, A., RAKIB, S., ORSZAG, S. A. & YAKHOT, V. 1989 Spectral element–RNG simulations of turbulent flows in complex geometries. In *Proc. Seventh Symp. on Turbulent Shear Flows, Stanford, CA.*

KIM, J. & MOIN, P. 1985 Applications of a fractional-step method to incompressible Navier–Stokes equations. *J. Comput. Phys.* **59**, 308.

KU, H. C., HIRSCH, R. S., TAYLOR, T. D. & ROSENBERG, A. P. 1989 A pseudospectral matrix element method for solution of three-dimensional incompressible flows and its parallel implementation. *J. Comput. Phys.* **83**, 260.

MADAY, Y. & PATERA, A. T. 1987 Spectral element methods for the Navier–Stokes equations. *State-of-the-art Surveys in Computational Mechanics*. ASME.

METCALFE, R. W., ORSZAG, S. A., BRACHET, M. E., MENON, S. & RILEY, J. J. 1987 Secondary instability of a temporally growing mixing layer. *J. Fluid Mech.* **184**, 207.

NEWHOUSE, S., RUELLE, D. & TAKENS, F. 1978 Occurrence of strange axiom A attractors near quasi periodic flows on $T^m, m > 3$. *Commun. Math. Phys.* **64**, 35.

ORSZAG, S. A. 1971 Accurate solution of the Orr–Sommerfeld stability equation. *J. Fluid Mech.* **50**, 689.

ORSZAG, S. A. & PATERA, A. T. 1983 Secondary instability of wall-bounded shear flows. *J. Fluid Mech.* **128**, 347.

OSSWALD, G. A., GHIA, K. N. & GHIA, U. 1983 Study of incompressible separated flow using an implicit time-dependent technique. In *AIAA, Sixth CFD Conf., Danvers, MA*, p. 686.

PATERA, A. T. 1984 A spectral element method for fluid dynamics; Laminar flow in a channel expansion. *J. Comput. Phys.* **54**, 468.

PIERREHUMBERT, R. T. & WIDNALL, S. E. 1982 The two- and three-dimensional instabilities of a spatially periodic shear layer. *J. Fluid Mech.* **114**, 59.

RONQUIST, E. M. 1988 Optimal spectral element methods for the unsteady three-dimensional incompressible Navier–Stokes equations. Ph.D. thesis, Massachusetts Institute of Technology.

SETHIAN, J. A. & GHONIEM, A. F. 1988 Validation study of vortex methods. *J. Comput. Phys.* **74**, 283.

TANI, I., INCHI, M. & KOMODA, H. 1967 Experimental investigation of flow separation associated with a step or groove. *Aero Res. Inst., Tokyo University, Rep.* 364, p. 119.

THANGHAM, S. & KNIGHT, D. D. 1989 Effect of stepheight on the separated flow past a backward-facing step. *Phys. Fluids* A **1**, 604.

TOMBOULIDES, A. G., ISRAELI, M. & KARNIADAKIS, G. E. 1991 Viscous sponge outflow boundary conditions for simulations of incompressible flows. *Minisymp. on Outflow Boundary Conditions, Stanford, CA*.

VOGEL, J. C. & EATON, J. K. 1984 Heat transfer and fluid mechanics measurements in the turbulent reattaching flow behind a backward-facing step. *Tech. Rep.* MD-44. Dept. of Mechanical Engineering, Stanford University.

YAKHOT, V. & ORSZAG, S. A. 1986 Renormalization group analysis of turbulence. I. Basic theory. *J. Sci. Comput.* **1**, 3.